

High Precision Astrometric Millimeter VLBI Using a New Method for Atmospheric Calibration.

M. Rioja^{1,2} and R. Dodson¹

¹ *ICRAR, UWA, Perth, Australia*

`maria.rioja@icrar.org`

ABSTRACT

We describe a new method which achieves high precision Very Long Baseline Interferometry (VLBI) astrometry in observations at millimeter wavelengths. It combines fast frequency-switching observations, to correct for the dominant non-dispersive tropospheric fluctuations, with slow source-switching observations, for the remaining ionospheric dispersive terms. We call this method Source-Frequency Phase Referencing. Provided that the switching cycles match the properties of the propagation media, one can recover the source astrometry.

We present an analytic description of the two-step calibration strategy, along with an error analysis to characterize its performance. Also, we provide observational demonstrations of a successful application with observations using the Very Long Baseline Array at 86 GHz of the pairs of sources 3C274 & 3C273 and 1308+326 & 1308+328, under various conditions.

We conclude that this method is widely applicable to millimeter VLBI observations of many target sources, and unique in providing *bona-fide* astrometrically registered images and high precision relative astrometric measurements in mm-VLBI using existing and newly built instruments.

Subject headings: Astrometry; techniques: interferometric; techniques: high angular resolution; methods: data analysis

1. Introduction

The comparative study of the radiation emitted at multiple radio bands has proved to be a useful tool in astronomy for the investigation of the nature of the emission mechanisms

²On secondment Observatorio Astronómico Nacional (OAN), Spain.

and to probe the physical conditions of the emitting regions. Multi-frequency observations with the high spatial resolution obtained with Very Long Baseline Interferometry (VLBI) are suitable for the study of extragalactic radio sources, such as AGNs, providing detailed images of the radiation from the relativistic jets, which are launched from the central engine that powers the sources. Observations at increasingly high frequencies offer the prospect of an increasingly deep exploration of the inner jet region, closer to the central engine.

By comparing well aligned high resolution images at multiple frequencies it is possible to map the spectral index across the jet structure. The spectral index map carries direct information about the physical conditions in the jet regions, and, potentially, with observations at the highest frequencies, on the structure of the central engine (Falcke et al. 2000). Also, the standard model (Blandford & Konigl 1979) predicts changes in the apparent position of the observed “core” component, at the base of the jet, in observations at different frequencies as a result of opacity effects in the jet. These position changes are called *core-shifts* and hold a direct relationship with the conditions in the nuclear region at the base of the jet where the “core” is located. For both studies the precise alignment of the source images is mandatory to assess true intrinsic source properties using multi-frequency comparison techniques, otherwise alignment errors will result in misleading conclusions.

Standard VLBI images, which are created using self-calibration techniques, provide exquisite detail on the source structure but lack astrometric information. The astrometry is lost in the process of removing the residual contributions arising from imprecise modeling of the propagation effects through the atmosphere and the use of independent frequency standards at each telescope, among others.

The special analysis technique of Phase Referencing (*hereafter* PR) is required to preserve the astrometric information. PR relies in the use of interleaving observations of an external calibrator source to correct the errors present in the target dataset, rather than using the target data themselves as in standard VLBI analysis (Alef 1988). By doing this it is possible to achieve high-precision (relative) *bona-fide* astrometric measurements of the angular separation between the two sources. The switching time and switching angle are critical parameters for the success of PR techniques. Typical switching values are estimated using the temporal and spatial structure-function of the atmospheric fluctuations, and are dependent on the observing frequency (Ulvestad 1999). Conventional phase referencing has been successfully used at cm-wavelengths (from 1.4 to 43-GHz) for which atmospheric effects are moderate and calibrator sources are easy to find.

VLBI observations at mm-wavelengths are challenging because of the lower sensitivity of the instruments, intrinsically lower source fluxes and shorter coherence times imposed by the rapid variations of the water vapor content in the troposphere. For the same reasons,

VLBI astrometry with conventional PR at high frequencies, beyond 43 GHz, is practically impossible due to the extremely short telescope switching times involved. The only successful demonstration was with the VLBA at 86-GHz for a pair of sources only 14' apart (Porcas & Rioja 2002, 2003).

An alternative approach to overcome the tropospheric limitations in observations at high frequencies consists in using fast frequency-switching, instead of fast source-switching as in PR, on the grounds that the tropospheric excess path delay, being independent of the observing frequency (i.e. it is a non-dispersive medium), can be corrected for using dual frequency observations. This technique has been attempted in VLBI resulting in longer effective coherence times at mm-wavelengths, but it failed to recover astrometry due to remaining dispersive ionospheric and instrumental errors (Middelberg et al. 2005).

We propose that astrometry at high frequencies can be achieved by combining alternating observations at two frequencies, to correct for the non-dispersive propagation media effects, and of two sources, to correct for the remaining dispersive effects, providing suitable switching times and switching angles are used. We term this new technique *Source-Frequency Phase Referencing* (hereafter SFPR). The direct outcomes of this technique are: high precision *bona-fide* astrometric measurements of the angular separation between emitting regions in the two frequency bands, and increased coherence time in VLBI observations at the highest frequencies. Hence it allows *bona-fide* astrometric registration of VLBI maps in the high frequency regime, beyond the threshold for conventional PR techniques. For example, applied to AGN-jets it would allow spectral index and core-shift measurements; applied to spectral line VLBI observations this would allow the alignment of the spatial distribution of emission arising from multiple maser transitions of a given molecule. Such information is of great interest in astrophysics (e.g. Lobanov (1998); Dodson et al. (2006); Soria-Ruiz et al. (2007); Rioja et al. (2008)). Moreover, the combination of SFPR and conventional PR techniques holds the prospect of providing high precision relative astrometric measurements of positions with respect to an external reference (i.e. a calibrator source). This would enable VLBI multi-epoch proper motion and parallax studies at the highest frequencies.

This paper presents an analytical description of this new technique that enables high precision VLBI astrometric measurements in the highest frequency regime, along with an experimental demonstration using VLBA observations at 43 and 86 GHz. Also, we present a comparative error analysis and discuss the feasibility of the new technique in the context of existing and newly built instruments. A comprehensive computer-simulation study of the SFPR performance will be presented elsewhere.

2. The Method

This section contains an analytic description of the basis of the SFPR astrometric technique. SFPR uses interleaving observations at a different frequency, and of a different source, to compensate for non-dispersive and dispersive errors, respectively, in the target observations. This approach resembles conventional PR techniques in the use of external observations to derive the calibration, rather than the target data themselves. SFPR can be applied to a wide range of frequencies, providing the switching cycles and switching angle match the fluctuations of the residual errors in the analysis. The frequency switching cycle (T_{swt}^ν) corresponds to the elapsed time between midpoints of two consecutive scans at the same frequency, and the source switching cycle (T_{swt}) is between blocks of scans on the same source. In the ideal case when multiple frequencies can be observed simultaneously ($T_{swt}^\nu=0$) only source switching is required. The switching angle is the angular separation between the two sources. Figure 1 describes the allocation of observing time, for each of the frequencies and sources, in SFPR observations. In this paper we will focus on the high frequency regime, where the dominant rapid tropospheric (non-dispersive) fluctuations prevent the application of conventional PR techniques, and SFPR is unique in its astrometric application. As a general rule, a fast frequency-switching cycle combined with a slow source-switching cycle is appropriate for SFPR observations at high frequencies. Section 4 contains detailed guidelines for planning such SFPR observations.

In order to simplify the presentation, we will use hereafter the term “target” to refer to both the source and frequency of interest; “reference frequency”, or simply “reference”, for the other frequency; “calibrator source”, or simply “calibrator”, for the other source. In the formulae, we will use the superscripts *high* and *low* to refer to the target and reference frequencies, respectively; and subscripts *A* and *B* for the target and calibrator sources, respectively.

The SFPR calibration strategy comprises of two steps. The first step (subsection 2.1) assumes that the dominant tropospheric residual errors (and in general, any non-dispersive errors) in the target dataset can be removed using the observations at a lower reference frequency, on the same source. The second step (subsection 2.2) assumes that the remaining ionospheric and instrumental errors (and in general, any other dispersive errors) can be removed using the interleaved observations of an external calibrator source. Finally, the nature of the astrometry enabled with this combined calibration technique is described in subsection 2.3.

2.1. Step 1: Calibration of Tropospheric errors using fast frequency-switching on the same source

The first SFPR calibration step uses fast-frequency switching observations, alternating between a lower reference frequency (ν^{low}) and a higher target frequency (ν^{high}), to compensate for the effect of errors in the tropospheric delay model at the target frequency. Such errors introduce an excess delay which is independent of the observing frequency (i.e. non-dispersive).

Our description of the SFPR method uses the residual phase VLBI observable, i.e. after the *a priori* model values for the various contributing terms have been removed at the correlation and the signal has been integrated, for each baseline. Following standard nomenclature the residual phase error values for observations of the target source (A) at the reference frequency, ϕ_A^{low} , are shown as a sum of contributions:

$$\phi_A^{\text{low}} = \phi_{A,\text{str}}^{\text{low}} + \phi_{A,\text{geo}}^{\text{low}} + \phi_{A,\text{tro}}^{\text{low}} + \phi_{A,\text{ion}}^{\text{low}} + \phi_{A,\text{inst}}^{\text{low}} + \phi_{A,\text{thermal}}^{\text{low}} + 2\pi n_A^{\text{low}}, \quad n_A^{\text{low}} \in \text{integer}, \quad (1)$$

where $\phi_{A,\text{geo}}^{\text{low}}$, $\phi_{A,\text{tro}}^{\text{low}}$, $\phi_{A,\text{ion}}^{\text{low}}$, and $\phi_{A,\text{inst}}^{\text{low}}$ are the contributions arising from geometric, tropospheric, ionospheric and instrumental inadequacies in the delay model, respectively. The $\phi_{A,\text{str}}^{\text{low}}$ term is the visibility phase, which accounts for the contribution of the source structure to the observed phases. Point-like source structures, and more generally symmetric structures, have $\phi_{A,\text{str}}^{\text{low}} = 0$. The $\phi_{A,\text{thermal}}^{\text{low}}$ term is the measurement error due to the sensitivity of the array, and is usually much smaller than the rest of the contributions. The $2\pi n_A^{\text{low}}$ term, with n_A^{low} an integer value, stands for the inherent modulo 2π phase ambiguity.

Similarly, for the target dataset, the residual phase error values for the interleaving observations of the target source at the target frequency, ϕ_A^{high} , are:

$$\phi_A^{\text{high}} = \phi_{A,\text{str}}^{\text{high}} + \phi_{A,\text{geo}}^{\text{high}} + \phi_{A,\text{tro}}^{\text{high}} + \phi_{A,\text{ion}}^{\text{high}} + \phi_{A,\text{inst}}^{\text{high}} + \phi_{A,\text{thermal}}^{\text{high}} + 2\pi n_A^{\text{high}},$$

with contributions as described above for Eq. 1, at the target frequency, ν^{high} . The tropospheric phase errors are proportional to the observing frequency, as for all non-dispersive media, and are the dominant contribution at the high frequencies. Instead, the dispersive ionospheric phase error is inversely proportional to the observing frequency, hence its effect becomes weaker as frequency increases.

The SFPR analysis starts by applying standard VLBI self-calibration and hybrid imaging techniques to the observations of the target source (A) at the reference frequency (ν^{low}).

This produces a map of the source along with a set of antenna-based terms, $\phi_{A,\text{self-cal}}^{\text{low}}$, that account for the sum of the errors in Eq. 1, except for $\phi_{A,\text{str}}^{\text{low}}$.

Next, these antenna-based corrections are interpolated to the interleaving scan times when the target frequency is observed, $\tilde{\phi}_{A,\text{self-cal}}^{\text{low}}$, and scaled by the frequency ratio R , with $R = \frac{\nu^{\text{high}}}{\nu^{\text{low}}}$. The resultant values, $R \cdot \tilde{\phi}_{A,\text{self-cal}}^{\text{low}}$, provide the basis for the tropospheric calibration of the target dataset. We call the resultant calibrated target dataset, using the interpolated plus scaled estimated solutions from the observations at the reference frequency, “Frequency Phase Transferred” (*hereafter* FPT), or *troposphere-free* target dataset. The corresponding residual target phases, ϕ_A^{FPT} , are:

$$\begin{aligned} \phi_A^{\text{FPT}} = & \phi_A^{\text{high}} - R \cdot \tilde{\phi}_{A,\text{self-cal}}^{\text{low}} = \phi_{A,\text{str}}^{\text{high}} \\ & + (\phi_{A,\text{geo}}^{\text{high}} - R \cdot \tilde{\phi}_{A,\text{geo}}^{\text{low}}) + (\phi_{A,\text{tro}}^{\text{high}} - R \cdot \tilde{\phi}_{A,\text{tro}}^{\text{low}}) \\ & + (\phi_{A,\text{ion}}^{\text{high}} - R \cdot \tilde{\phi}_{A,\text{ion}}^{\text{low}}) + (\phi_{A,\text{inst}}^{\text{high}} - R \cdot \tilde{\phi}_{A,\text{inst}}^{\text{low}}) \\ & + 2\pi(n_A^{\text{high}} - R \cdot n_A^{\text{low}}), \end{aligned} \quad (2)$$

where we have omitted the thermal noise term, for simplicity.

At this point we can make some reasonable approximations concerning the difference terms in brackets in Eq. 2. First, given that the tropospheric residual phase errors scale linearly with frequency, and providing that the frequency switching cycle used is suitable to sample the rapid tropospheric fluctuations then:

$$\phi_{A,\text{tro}}^{\text{high}} - R \cdot \tilde{\phi}_{A,\text{tro}}^{\text{low}} \approx 0,$$

Second, given that the geometric errors are also non-dispersive, the effect of any errors in the antenna and source coordinates will effectively cancel out using this calibration procedure, except for a frequency-dependent source position shift, such as core-shift phenomena in AGNs, but in general any change in position between the frequency bands irrespective of its nature. We refer to all of these as “core-shifts” *hereafter*:

$$\phi_{A,\text{geo}}^{\text{high}} - R \cdot \tilde{\phi}_{A,\text{geo}}^{\text{low}} \approx 2\pi \vec{D}_{\lambda^{\text{high}}} \cdot \vec{\theta}_A,$$

where $\vec{\theta}_A$ stands for the target source “core-shift” between the two observed frequencies, and $\vec{D}_{\lambda^{\text{high}}}$ is the interferometer baseline vector in units of λ^{high} wavelengths, with $\lambda^{\text{high}} = c/\nu^{\text{high}}$.

However, the dispersive residual errors in the target dataset will not be compensated using this calibration procedure. The ionospheric and instrumental residual phase errors belong to this category, and therefore remaining residuals are expected:

$$\phi_{A,\text{ion}}^{\text{high}} - R \cdot \tilde{\phi}_{A,\text{ion}}^{\text{low}} \approx \left(\frac{1}{R} - R\right) \tilde{\phi}_{A,\text{ion}}^{\text{low}} \quad (3)$$

$$\phi_{A,\text{inst}}^{\text{high}} - R \cdot \tilde{\phi}_{A,\text{inst}}^{\text{low}} \neq 0.$$

Making use of the approximations described above, Eq. 2 becomes:

$$\phi_A^{\text{FPT}} = \phi_{A,\text{str}}^{\text{high}} + 2\pi \vec{D}_{\lambda^{\text{high}}} \cdot \vec{\theta}_A + \left(\frac{1}{R} - R\right) \tilde{\phi}_{A,\text{ion}}^{\text{low}} + (\phi_{A,\text{inst}}^{\text{high}} - R \cdot \tilde{\phi}_{A,\text{inst}}^{\text{low}}) + \Delta_{i,T_{\text{swt}}^{\nu}}, \quad R \in \text{integer}, \quad (4)$$

where $\Delta_{i,T_{\text{swt}}^{\nu}}$ stands for the interpolation errors arising from using a frequency switching cycle T_{swt}^{ν} . Note that with simultaneous dual frequency observations, for example using the Korean VLBI Network (KVN) (Kim et al. 2007), no interpolation is required and $\Delta_{i,T_{\text{swt}}^{\nu}}=0$. For simplicity we have omitted the 2π phase ambiguity term in Eq. 4 which, providing R is an integer value, just adds an unknown number of complete turns and is irrelevant for the analysis. The importance of having an integer ratio between the frequencies involved in SFPR calibration is discussed in Section 4.

Eq. 4 shows that the FPT-calibrated target dataset is free of the random and systematic tropospheric errors, providing a suitably fast frequency-switching cycle was used at the observations. However, contaminating long-term ionospheric and instrumental residual phase variations still remain blended with the source structure and the astrometric “core-shift” signature, preventing its direct extraction. At this point, previous realizations of the dual-frequency VLBI calibration method applied self-calibration techniques on the FPT-calibrated target dataset to eliminate the contaminating terms, with the consequent loss of the astrometric information (Middelberg et al. 2005; Jung et al. 2008).

We propose instead an alternative calibration strategy which preserves the chromatic astrometry signature (i.e. the “core-shift” information). This is described in the next section.

2.2. Step 2: Calibration of Ionospheric errors using slow telescope-switching between two sources.

The second SFPR calibration step uses the observations of an external calibrator source (B) to eliminate the remaining dispersive errors in Eq. 4, in a similar fashion as in conventional phase referencing. The observations of the calibrator and the target sources are interleaved using a much slower switching cycle than that required for conventional phase referencing. A discussion on the constraints on the source switching cycle and the switching angle is presented in Section 4. The observations of the calibrator source are carried out using fast-frequency switching scans, as described for the target source, and analyzed following the same procedures as described in section 2.1 for the target source. Therefore, the tropospheric-free residual phases for the calibrator source, ϕ_B^{FPT} , can be expressed, following Eq. 4, as:

$$\phi_B^{\text{FPT}} = 2\pi \vec{D}_{\lambda^{\text{high}}} \cdot \vec{\theta}_B + \left(\frac{1}{R} - R\right) \tilde{\phi}_{B,\text{ion}}^{\text{low}} + (\phi_{B,\text{inst}}^{\text{high}} - R \cdot \tilde{\phi}_{B,\text{inst}}^{\text{low}}) + \Delta_{i,T^\nu_{\text{swt}}}, \quad (5)$$

where $\vec{\theta}_B$ is the “core-shift” in the calibrator, and the rest of the terms are similar to those described in Eq. 4, but for the calibrator source. We assume a compact calibrator source, i.e. $\phi_{B,\text{str}}^{\text{high}} = 0$; in general one should correct for the structure term, $\phi_{B,\text{str}}^{\text{high}}$, using the calibrator hybrid map.

It is reasonable to assume that the tropospheric-free calibrator dataset (Eq. 5) could be used to remove the remaining errors in the tropospheric-free target dataset (Eq. 4), as done in conventional PR analysis. This is the essence of the *Step 2* calibration. We dubbed the resultant differenced values the “SFPR-calibrated” dataset.

The conditions under which the *Step 2* calibration works are:

a) that the source switching cycle is faster than the residual ionospheric fluctuations at the reference frequency, and *b)* that the angular separation between the calibrator and target sources is smaller than the ionospheric isoplanatic patch-size at the reference frequency, which is defined as the area over which the variation of excess phase due to the ionosphere is small compared with 2π radians, hence:

$$\left(\frac{1}{R} - R\right) \tilde{\phi}_{A,\text{ion}}^{\text{low}} \approx \left(\frac{1}{R} - R\right) \tilde{\phi}_{B,\text{ion}}^{\text{low}}$$

and *c)*, that the instrumental phase errors, due to independent frequency standards and electronic equipment at each antenna, are common for the observations of the target and calibrator sources, then:

$$\phi_{A,\text{inst}}^{\text{high}} - R \cdot \tilde{\phi}_{A,\text{inst}}^{\text{low}} \approx \phi_{B,\text{inst}}^{\text{high}} - R \cdot \tilde{\phi}_{B,\text{inst}}^{\text{low}}. \quad (6)$$

This is described in more detail in Section 3.2

These conditions are far less restrictive than the ones that apply for conventional PR techniques, and can be easily met using source-switching cycles up to \sim several minutes, and switching angles up to \sim several degrees for SFPR observations at high frequencies (further details are to be found in Section 4).

Making use of these approximations, the SFPR-calibrated visibility phases of the target dataset, ϕ_A^{SFPR} , are:

$$\phi_A^{\text{SFPR}} = \phi_{A,\text{str}}^{\text{high}} + 2\pi \vec{D}_{\lambda^{\text{high}}} \cdot (\vec{\theta}_A - \vec{\theta}_B) + \Delta_{i,T_{\text{swt}}^\nu} + \Delta_{i,T_{\text{swt}}}, \quad (7)$$

where $\Delta_{i,T_{\text{swt}}}$ stands for the interpolation errors arising from using a source switching cycle T_{swt} . The SFPR-calibrated phases are free of tropospheric, ionospheric and instrumental corruption, while keeping the chromatic astrometry signature. The terms $2\pi \vec{D}_{\lambda^{\text{high}}} \cdot \vec{\theta}_A$ and $2\pi \vec{D}_{\lambda^{\text{high}}} \cdot \vec{\theta}_B$ modulate the phase residuals for each baseline with ~ 24 hours period sinusoid whose amplitude depends on the magnitude of the “core-shifts” in A and B, respectively. It is interesting to note that the “core-shift” functional dependence in Eq. 7 is identical to that for the pair angular separation in conventional PR, although the latter can not be applied at high frequencies. The propagation of interpolation errors into the SFPR analysis is addressed in the error analysis in Section 3.

2.3. Outcomes of SFPR

This section is concerned with the outcomes of the SFPR technique: high sensitivity source maps and precise astrometric measurements at the highest frequencies. The SFPR-calibrated target dataset (see Eq. 7) is Fourier inverted and deconvolved to yield a synthesis image of the target source at the target frequency (ν^{high}). We call this the SFPR-map. The effective coherence time of the SFPR-calibrated dataset is increased as a result of the tropospheric calibration derived with fast-frequency switching observations, and further improved after the ionospheric and instrumental calibration using the observations of a calibrator source. The result is a lower detection threshold for the SFPR observations at ν^{high} . This technique is therefore suitable for the detection of weak sources, even at the high frequencies

beyond the applicability of conventional phase referencing techniques as demonstrated in Middelberg et al. (2005).

SFPR observations on their own enable *bona-fide* “chromatic” astrometry, that is, measurements of frequency-dependent source position shifts. Eq. 7 shows that the SFPR-calibrated phases are sensitive to “core-shifts” in the target and the calibrator sources, which can be measured directly in the SFPR-map. Given the similarity between the functional dependence of “core-shifts” and source pair separation in the calibrated datasets using SFPR and PR techniques, respectively, it is easy to see that these can be measured in the SFPR-map in a similar way as angular separations are measured in PR maps. That is, the position offset of the target source relative to the SFPR-map center corresponds to a *bona-fide* high precision astrometric measurement of the relative “core shifts” in the calibrator and target sources between the two observed frequencies.

The combination of SFPR observations, at ν^{low} and ν^{high} , and PR observations at ν^{low} , enables relative astrometry (i.e. measurement of the target source position with respect to an external reference frame) at ν^{high} . Therefore it is possible to achieve relative astrometric measurements at the highest frequencies, beyond the ~ 43 -GHz upper limit in conventional PR techniques. The requirements for the switching cycles and the calibrator source in SFPR observations are relatively easy to fulfill, hence are compatible with a wide range of targets and applications. Performing multi-epoch observations will enable high precision parallax and proper motion studies at the highest frequencies.

3. Error Analysis

This section is concerned with the propagation of errors in the VLBI observables listed in Eq. 1, and from the interpolation process, into the astrometric estimates using SFPR calibration techniques. To simplify the presentation, the individual sources of errors are grouped into subsections 3.1 and 3.2 according to their dispersion properties, or equivalently, to their compensation within the *Step 1* or *Step 2* interpolation process in the SFPR calibration strategy. The third subsection 3.3 is devoted to the thermal noise error contribution.

The propagation of the spatial and temporal interpolation errors in the data analysis using conventional PR techniques has been studied thoroughly using analytical and simulation studies (Shapiro et al. 1979; Beasley & Conway 1995; Fomalont 1995; Pradel et al. 2006; Asaki et al. 2007). Here, we present an analytical study of the errors in SFPR techniques based on a modified version of the error analysis for conventional PR techniques presented in Asaki et al. (2007) (*hereafter* A07).

3.1. *Non-dispersive Terms: Tropospheric and Geometric errors (Step 1)*

The dominant contribution to the VLBI tropospheric errors arise from inadequately modeling the inhomogeneous and highly variable distribution of water vapor content, the so-called *wet* part, in the troposphere. Typical values of the equivalent tropospheric zenith excess path delay are $\sim 3\text{--}5$ cm, for each telescope, and have a non-dispersive nature. The VLBI tropospheric errors exhibit random or semi-random temporal fluctuations, which limit the coherence times, and quasi temporally-invariant spatial variations along different sight line directions. They are referred to as the *dynamic* and *static* components of the troposphere, respectively.

To correct for the VLBI tropospheric errors, and in general for any errors, conventional PR uses fast source-switching observations and the interpolation between scans of a calibrator source to the target source scans, which is along a different line of sight. After correcting for the interpolated residual values the remaining errors in the target dataset are attenuated, by a factor which is inversely proportional to the source pair angular separation, but can still be significant. At frequencies above ~ 10 GHz, the dominant source of errors in the astrometric estimates are the uncertainties in the tropospheric delay model, even when using a nearby ($\sim 1^\circ$ away) calibrator source as shown in the simulation work of Pradel et al. (2006) and A07. Using simultaneous observations of the sources, i.e. with VERA (Honma et al. 2003), results in an improved compensation of the errors arising from the *dynamic* component of the troposphere, but those from the *static* component still remain, and pose a limit in the achievable astrometric precision, irrespective of the observing frequency. In order to achieve the very highest astrometric precision additional independent measurements to reduce the *static* tropospheric errors are required (Reid & Brunthaler 2004; Honma et al. 2008).

Instead, the SFPR technique *Step 1* corrects the tropospheric errors in the target dataset using fast frequency-switching observations of the same source plus interpolation between scans at the reference frequency to calibrate the target frequency scans, along the same line of sight, after scaling by the frequency ratio.

Having observations along the same line-of-sight offers considerable advantages for the precise calibration of the *static* tropospheric errors, as shown below. Additionally, in the ideal case of simultaneous dual frequency observations the need for interpolation between consecutive scans at the reference frequency is eliminated and an exact calibration of the *dynamic* component of the troposphere can be achieved as well.

Taking into account the similarity between the two calibration techniques, we propose to use a modified version of the formulae in A07 for conventional PR, to characterize the propagation of non-dispersive errors in SFPR. These modifications of the formulae consist

of *a*) replacing the source switching cycle in PR by the frequency switching cycle in SFPR, *b*) replacing the source pair angular separation in PR, by the “core-shift” values between the two frequencies in SFPR, *c*) adding a multiplicative factor equal to the SFPR frequency ratio R to give the phase errors at the target frequency (ν^{high}), whilst using the reference frequency (ν^{low}) in the formula, and *d*) adding a multiplicative factor of $\sqrt{2}$ to adapt for ground-ground rather than space-ground baselines, as used in A07.

By doing this, the estimated SFPR residual phase error at the target frequency (ν^{high}) due to the *dynamic* component of the troposphere, $\sigma\phi_{\text{dtrp}}^{\text{high}}$, for dual frequency observations of source A, with a given baseline, becomes:

$$\begin{aligned} \sigma\phi_{\text{dtrp}}^{\text{high}}[\text{deg}] &\approx \sqrt{2} R 27 C_w \left(\frac{\nu^{\text{low}}[\text{GHz}]}{43\text{GHz}} \right) \left(\frac{\sec Z_g}{\sec 45^\circ} \right)^{1/2} \times \left(\frac{T_{\text{swt}}^\nu[\text{s}]}{60\text{s}} + 0.16 \left(\frac{\sec Z_g}{\sec 45^\circ} \right) \left(\frac{\theta_A[^\circ]}{2^\circ} \right) \right)^{5/6} \\ &\approx R 38 C_w \left(\frac{\nu^{\text{low}}[\text{GHz}]}{43\text{GHz}} \right) \left(\frac{\sec Z_g}{\sec 45^\circ} \right)^{1/2} \times \left(\frac{T_{\text{swt}}^\nu[\text{s}]}{60\text{s}} \right)^{5/6}, \quad (8) \end{aligned}$$

where ν^{low} is the reference frequency, T_{swt}^ν is the frequency switching cycle, C_w is a modified coefficient of the troposphere spatial structure function to characterize the weather conditions (with values 1, 2, and 4 for good, typical and poor tropospheric conditions, respectively), and Z_g is the telescope zenith angle. θ_A stands for the magnitude of the “core-shift” between ν^{low} and ν^{high} which for AGNs for example, has typical values of a few hundreds of μas at centimeter wavelengths, and is expected to be reduced at higher frequencies. The random phase noise introduced by the short-term tropospheric fluctuations is expected to affect the quality of the map by producing blurred images, but not shifts of the peak of brightness that lead to astrometric errors. Eq. 8 shows that such turbulence errors can be attenuated using fast frequency switching cycles. Ultimately, note that these errors become zero in the case of simultaneous ($T_{\text{swt}}^\nu=0$) dual frequency observations. Table 1 lists the estimated $\sigma\phi_{\text{dtrp}}^{\text{high}}$ residual phase values using both fast frequency switching and simultaneous dual frequency observations for two pairs of frequencies, namely 43/86 GHz and 43/129 GHz, with typical observing parameters for SFPR; for comparison, the estimated values for conventional PR at 43 GHz are also listed.

Similarly, the SFPR residual errors at ν^{high} due to the *static* component of the troposphere, $\sigma\phi_{\text{strp}}^{\text{high}}$, are expressed as:

$$\sigma\phi_{\text{strp}}^{\text{high}}[\text{deg}] \approx \sqrt{2} R 76 \left(\frac{\nu^{\text{low}}[\text{GHz}]}{43\text{GHz}} \right) \left(\frac{\Delta l_z[\text{cm}]}{3\text{cm}} \right) \left(\frac{\theta_A[^\circ]}{2^\circ} \right) \left(\frac{\cos Z_g}{\cos 45^\circ} \right)^{-1} \left(\frac{\tan Z_g}{\tan 45^\circ} \right) \approx 0, \quad (9)$$

where Δl_z is the uncertainty in the tropospheric zenith excess path length (typical values, $\sim 3\text{--}5$ cm). All the systematic (or *static*) errors are strongly attenuated by the small magnitude of the “core-shift” (θ_A) parameter. For comparison, the attenuation factor resulting from a typical AGN core-shift value in SFPR observations is more than 10^7 times greater than that in PR observations of a pair of sources with $\sim 1^\circ$ separation. These systematic errors set a barrier in the astrometric precision achievable with conventional PR techniques, as mentioned above. Instead, they are completely suppressed in SFPR techniques due to the same line-of-sight dual frequency observations (except for the effectively zero angular separation due to the “core-shift”). Table 1 lists the estimated $\sigma\phi_{\text{strp}}^{\text{high}}$ residual phase values for typical observing parameters with SFPR observations; for comparison, the estimated values using conventional PR at 43 GHz are included.

For the same reason the errors arising from any inadequacies in the “a priori” geometric delay model, comprising errors in the source position ($\sigma\phi_{\Delta s}$) and antennae coordinates ($\sigma\phi_{\text{bl}}$), among others, are also readily compensated in *Step 1*.

$$\sigma\phi_{\Delta s}^{\text{high}}[\text{deg}] \approx R 16 \left(\frac{\nu^{\text{low}}[\text{GHz}]}{43\text{GHz}} \right) \left(\frac{B[\text{km}]}{6000\text{km}} \right) \left(\frac{\Delta s^c[\text{mas}]}{0.3\text{mas}} \right) \times \left(\frac{\theta_A[\text{deg}]}{2^\circ} \right) \approx 0,$$

$$\sigma\phi_{\text{bl}}^{\text{high}}[\text{deg}] \approx R 18 \left(\frac{\nu^{\text{low}}[\text{GHz}]}{43\text{GHz}} \right) \left(\frac{\Delta P[\text{cm}]}{1\text{cm}} \right) \times \left(\frac{\theta_A[\text{deg}]}{2^\circ} \right) \approx 0,$$

where Δs^c is the source position error, B is the projected baseline length, and ΔP represents the combined contribution from the Earth Orientation Parameters and both the antenna coordinate errors. Table 1 lists the estimated values for $\sigma\phi_{\text{geo}}^{\text{high}}$ which is comprised of the terms above.

Summarizing, the propagation of systematic tropospheric errors (*static* component) into the estimates using SFPR calibration techniques is negligible because of the attenuation from the near-identical lines of sight for the two observing frequencies, and the same applies to geometric errors. Furthermore the short-term tropospheric errors (*dynamic* component) will effectively cancel with simultaneous dual frequency observations, since $T_{\text{swt}}^\nu = 0$. Therefore, the capability for simultaneous multiple frequency-band observations, with arrays like KVN and telescopes like Yebes and Haystack, gives an exact adaptive tropospheric correction using SFPR techniques. The advantage of this being an extended coherence time (at the target frequency), so a greater number of weaker sources will be detectable by means of longer integration times, as well as the improved quality of the SFPR-map and more accurate astrometric measurements.

3.2. Dispersive Terms: Ionospheric and Instrumental errors (*Step 2*)

The inaccuracies in the ionospheric delay model introduce a dispersive phase error which is inversely proportional to the observing frequency. The effect of the ionospheric errors is conveniently described as a compound of *static* and *dynamic* components, similar to the description for the troposphere. The latter introduces temporal phase fluctuations caused by the irregularities in the plasma density in the ionosphere; the former introduces quasi temporally invariant spatial variations arising from uncertainties in the vertical total electron content (TEC) and the geometry of the atmosphere.

Although the ionospheric effects at the high frequencies of interest for this paper are expected to be weak, and are certainly much smaller than the tropospheric errors, they still need to be accounted for. Attempts to achieve astrometry using only fast-frequency switching strategies failed because those were not corrected for (Middelberg et al. 2005).

Calibration *Step 2* of the SFPR technique corrects the tropospheric-free target dataset for ionospheric errors by using interleaved observations of an external calibrator source, and interpolation to the target source scans, following a similar strategy as in conventional PR. Despite its similarity to PR, the constraints on the source switching cycle and the angular separation between the sources are much less strict in SFPR due to the preceding tropospheric calibration (*Step 1*). It should be noted that a side effect of the tropospheric calibration is that the effective residual ionospheric errors at the target frequency are those at the reference frequency, ν^{low} , multiplied by a factor $R - 1/R$ (see Eq. 3); hence the ionospheric time and space coherence (i.e. the ionospheric isoplanatic patch size) are effectively reduced by a similar factor. However these are still much less significant than the dominant tropospheric errors in conventional PR.

Taking this into account, we propose a modified version of the A07 formula that describes the interpolated SFPR residual phase errors at the target frequency (ν^{high}) introduced by the *dynamic* ionosphere, $\sigma\phi_{\text{dion}}^{\nu^{\text{high}}}$:

$$\begin{aligned} \sigma\phi_{\text{dion}}^{\text{high}}[\text{deg}] \approx & \sqrt{2} (R - 1/R) 0.46 \left(\frac{\sec Z_i}{\sec 43^\circ} \right)^{1/2} \left(\frac{\nu^{\text{low}}[\text{GHz}]}{43\text{GHz}} \right)^{-1} \\ & \times \left[0.21 \left(\frac{T_{\text{swt}}[\text{s}]}{60\text{s}} \right) + \left(\frac{\sec Z_i}{\sec 43^\circ} \right) \left(\frac{\Delta\theta[^\circ]}{2^\circ} \right) \right]^{5/6}, \end{aligned} \quad (10)$$

where T_{swt} is the source-switching cycle between the target and calibrator sources, $\Delta\theta$ is their angular separation (i.e. switching angle), and Z_i is the zenith angle measured at an altitude of ~ 300 km (bottom of the ionospheric F-region) which corresponds to the height

of the phase screen model of the ionospheric propagation effects. Table 1 lists the estimated $\sigma\phi_{\text{dion}}^{\text{high}}$ residual phase values, for observations at 43/86GHz and at 43/129 GHz, using two source pair angular separations, equal to 2 and 10 degrees, and a source-switching cycle of 5 minutes. Based on these estimates, the effect of the residual ionospheric random phase noise (introduced by the short-term ionospheric fluctuations) on the quality of the SFPR-ed map is negligible at the high frequencies of interest for this paper.

Similarly, the interpolated SFPR residual phase errors arising from the *static* component of the ionosphere can be expressed as:

$$\sigma\phi_{\text{sion}}^{\text{high}}[\text{deg}] \approx \sqrt{2} (R - 1/R) 2.7 \left(\frac{\nu^{\text{low}}[\text{GHz}]}{43\text{GHz}} \right)^{-1} \left(\frac{\Delta I_V[\text{TECU}]}{6\text{TECU}} \right) \left(\frac{\Delta\theta[\text{deg}]}{2^\circ} \right) \times \left(\frac{\cos Z_F}{\cos 41^\circ} \right)^{-1} \left(\frac{\tan Z_F}{\tan 41^\circ} \right), \quad (11)$$

where ΔI_V is the systematic error in the estimate of the vertical TEC, TECU is the TEC unit (10^{16} electrons m^{-2}), and Z_F is the zenith angle measured at the altitude of the electron density peak (typically, 450 km).

The propagation of long-term systematic ionospheric errors is attenuated by a factor proportional to the source pair angular separation, expressed in radians, and its value can be large for wide switching angles.

Such long-term phase errors can distort the image and affect the astrometric measurements in the SFPR-ed map. In SFPR observations, which provide a quasi perfect compensation of systematic tropospheric errors, the ionospheric errors can become the dominant source of astrometric errors.

Table 1 lists the estimated $\sigma\phi_{\text{sion}}^{\text{high}}$ residual phase values, for observations at 43/86GHz and at 43/129 GHz, using source pair angular separations of 2 and 10 degrees, and a source-switching cycle of 5 minutes. Based on these estimates, at the high frequency regime of interest in this paper, source-switching cycles of several minutes, and switching angles up to 10 degrees, or even larger, are acceptable for SFPR observations.

The residual instrumental phase errors in Eq. 2 are also compensated in the *Step 2* calibration, along with the ionospheric errors. These contributions arise from the excess path introduced by the electronics and independent frequency standards and elevation-dependent structure deformations at each antenna. Albeit difficult to estimate, such contributions are expected to be slowly varying with time, as a result of changes of ambient conditions and with observing elevation angles. Therefore, a slow source switching cycle of several minutes,

as required for the compensation of ionospheric errors, is suitable to compensate for the instrumental errors as well (i.e. $\phi_{A,\text{inst}}^{\text{high}} \approx \phi_{B,\text{inst}}^{\text{high}}$; $\tilde{\phi}_{A,\text{inst}}^{\text{low}} \approx \tilde{\phi}_{B,\text{inst}}^{\text{low}}$), and meet the working condition for *Step 2* expressed in Eq. 6. Hence, the instrumental errors in SFPR $\sigma\phi_{\text{inst}}$ are negligible:

$$\sigma\phi_{\text{inst}} = \left(\phi_{A,\text{inst}}^{\text{high}} - R \cdot \tilde{\phi}_{A,\text{inst}}^{\text{low}} \right) - \left(\phi_{B,\text{inst}}^{\text{high}} - R \cdot \tilde{\phi}_{B,\text{inst}}^{\text{low}} \right) \approx 0.$$

3.3. Thermal Noise

The thermal noise in the VLBI observables sets the final insurmountable barrier to the map quality and the astrometric precision, in the absence of other sources of errors.

The general expression for the error in the phase measurements with a pair of antennas i and j due to thermal noise is given by:

$$\sigma\phi_{\text{thermal}}[\text{rad}] = \Delta S_{i,j}/S = \frac{1}{\eta_s} \sqrt{\frac{\text{SEFD}_i[\text{Jy}] \times \text{SEFD}_j[\text{Jy}]}{2\Delta\nu[\text{Hz}]T[\text{sec}]} \frac{1}{S[\text{Jy}]}} ,$$

from Walker (1995), where $\Delta S_{i,j}$ is the detection threshold for the baseline and S is the source flux. $\text{SEFD} = T_{\text{sys}}/G$ (with T_{sys} the system temperature, and G the antenna gain) is the antenna's system equivalent flux density, a parameter that measures the overall performance of each antenna, η_s is the interferometer system efficiency which accounts for digital losses, T is the integration time, and $\Delta\nu$ is the bandwidth collected at each antenna,

An equivalent expression for two-bit data sampling, as given by A07, is:

$$\sigma\phi_{\text{thermal}}[\text{deg}] = 1.6 \times 10^{-5} \left(\frac{\Delta\nu[\text{MHz}]}{256\text{MHz}} \right)^{-1/2} \left(\frac{T[\text{s}]}{10\text{s}} \right)^{-1/2} \left(\frac{\overline{\text{SEFD}}[\text{Jy}]}{S[\text{Jy}]} \right), \quad (12)$$

where $\overline{\text{SEFD}}$ stands for the geometric mean of the SEFD values for the two antennas.

An expression for the thermal noise phase error resulting from the *Step 1* calibration in SFPR techniques can be written as:

$$\sigma\phi_{A,\text{thermal}}^{\nu^{\text{low}},\nu^{\text{high}}} = \sqrt{[\sigma\phi_{A,\text{thermal}}^{\nu^{\text{high}}}]^2 + \frac{R^2}{2} [\sigma\phi_{A,\text{thermal}}^{\nu^{\text{low}}}]^2} ,$$

where $\sigma\phi_{A,\text{thermal}}^{\nu^{\text{high}}}$ and $\sigma\phi_{A,\text{thermal}}^{\nu^{\text{low}}}$ stand for the thermal noise error in the phase measurements at the target (ν^{high}) and reference (ν^{low}) observing frequencies, respectively, of source

A, as given by Eq. 12. The factor $\sqrt{\frac{R^2}{2}}$, where $R = \nu^{\text{high}}/\nu^{\text{low}}$, comes from the scaling and interpolation operations between consecutive reference frequency scans to calibrate the interleaving scan at the target frequency, on a common source. An identical expression applies for the observations of source B, $\sigma\phi_{\text{B,thermal}}^{\nu^{\text{low}},\nu^{\text{high}}}$.

Similarly, an expression for the thermal noise phase error resulting from the *Step 2* calibration can be written as:

$$\sigma\phi_{\text{A,B,thermal}}^{\nu^{\text{high}}} = \sqrt{[\sigma\phi_{\text{A,thermal}}^{\nu^{\text{high}}}]^2 + \frac{1}{2}[\sigma\phi_{\text{B,thermal}}^{\nu^{\text{high}}}]^2},$$

where $\sigma\phi_{\text{A,thermal}}^{\nu^{\text{high}}}$ and $\sigma\phi_{\text{B,thermal}}^{\nu^{\text{high}}}$ are given by Eq. 12, and the factor $\frac{1}{\sqrt{2}}$ results from the interpolation between consecutive calibrator source (B) scans to calibrate the target source (A) scans in-between. Note that the integration time in *Step 2* calibration is extended beyond the nominal coherence time at ν^{high} as a result of the preceding tropospheric calibration.

Finally, the thermal phase noise contribution using SFPR techniques, for a baseline, can be expressed as the root sum square of the contributions above, that is:

$$\sigma\phi_{\text{SFPR,thermal}}^{\text{high}} = \sqrt{(\sigma\phi_{\text{A,thermal}}^{\nu^{\text{low}},\nu^{\text{high}}})^2 + (\sigma\phi_{\text{B,thermal}}^{\nu^{\text{low}},\nu^{\text{high}}})^2 + (\sigma\phi_{\text{A,B,thermal}}^{\nu^{\text{high}}})^2}.$$

Taking typical SEFD parameter for the VLBA antennas at 43 and 86 GHz, and source fluxes equal to 0.1 Jy with a bandwidth of 256 MHz and integration time of 10 seconds, the value of $\sigma\phi_{\text{SFPR,thermal}}$ is $\sim 1.5^\circ$ at 86 GHz. In general, this contribution is insignificant compared to other sources of errors in the astrometric analysis. Nevertheless using SFPR techniques, with simultaneous dual-frequency observations, one would approach the thermal limits at sub-millimeter wavelengths.

4. Guidelines for Scheduling SFPR Observations

This section provides practical guidelines for scheduling SFPR observations from a perspective of minimizing the analysis errors.

4.1. Integer frequency ratio and magnitude of R

In general, it is strongly recommended that the two frequencies involved in the SFPR technique have an integer ratio in order to avoid phase-ambiguity related problems in the analysis. Such phase-ambiguity issues arise from the inherent unknown number of 2π cycles in the measured phase values, as shown in Eq. 2. The scaling by the frequency ratio R

involved in the *Step 1* calibration of SFPR will continue to keep this unknown term as a whole number of cycles, and transparent to the analysis, as long as the scaling factor is an integer number. Note that it is sufficient that the recorded bandwidths cover the frequencies with an integer ratio. Preliminary results from our simulations suggest that extrapolation to a frequency value outside the covered band might be feasible in certain cases, nevertheless further investigation is required and results will be reported somewhere else. Non-integer frequency ratios will, in general, introduce phase offsets and jumps which would have to be addressed separately. The exception to that being the rare case when the number of phase turns is the same for both sources, as for example in observations of the extremely nearby quasar pair 1038+528 A and B, 33'' apart as demonstrated in Rioja et al. (2005).

The value of R , besides being integer, has an impact on the ionospheric phase compensation, as shown in Eq. 3. For a given target frequency, the magnitude of the residual ionospheric phase errors will increase with larger values of R , or equivalently lower reference frequency. The reason for this is twofold, first, due to the increased ionospheric effects at lower reference frequencies, and second, due to the multiplicative factor $(R - 1/R)$. Instead, the magnitude of the non-dispersive errors is independent of the value of R . As for the thermal noise errors the combined effect of R , the receiver noise (SEFD) and the source fluxes must be considered on a case-to-case basis, but are generally much smaller than the ionospheric effect.

Therefore, the advantages of using as the reference frequency a lower frequency, such as better receiver performance, higher intrinsic source flux and longer coherence times, should be balanced against the issues raised by the propagation of increased ionospheric effects at lower frequencies, further amplified by the $R - 1/R$ factor in the SFPR analysis. As a compromise, in absence of other reasons to choose the observing frequencies, we generally recommend the use of a reference frequency equal to 22 GHz or above (whilst avoiding 22.35 GHz where water absorption is problematic), where ionospheric effects start to be weak and the receiver performance is good.

4.2. *Switching times and Switching angle*

The dual frequency observations are the basis of the “*Step 1*” calibration in the SFPR technique. They enable an adaptive phase-based calibration of the tropospheric fluctuations at the target frequency using fast frequency switching observations of a common source. The frequency switching cycle has to be fast enough to fully sample the tropospheric fluctuations and ensure unambiguous phase connection between consecutive scans at the reference frequency. Without a reliable phase connection it is not possible to proceed any further in the

calibration therefore this is the most critical consideration in the scheduling.

At frequencies ≥ 10 -GHz the temporal variations in the residual phases are dominated by the random fluctuations that arise in the dynamic component of the troposphere. Therefore, the dynamic troposphere is the determining factor on setting the frequency-switching cycles at the frequencies of interest for SFPR. As a rule of thumb the same guidelines for telescope switching cycles in conventional PR at the reference frequency ν^{low} (see Beasley & Conway (1995); Ulvestad (1999)), including the weather dependence, apply for the frequency-switching cycles with SFPR. Those range between one and several minutes for observations at 22 GHz under typical and good weather conditions; for 43 GHz, between several tenths of a minute to a few minutes. Also, the switching cycle has to allow for direct detections of both sources at the reference frequency, as explained below in subsection 4.3.

Having a fast frequency switching cycle reduces the magnitude of (random) tropospheric errors, as shown in Eq. 8, which result in a blurring effect. Ultimately, by using simultaneous observations at multiple frequencies, as the KVN will do, this error term will vanish completely. Other advantages are that since a tropospheric interpolation would not be required phase connection is not an issue, and the increased on-source time means that weaker sources would be suitable for SFPR observations.

The source switching strategy is the basis of the *Step 2* calibration in SFPR techniques to compensate for remaining ionospheric and instrumental effects, after the tropospheric effects have been removed. The ionospheric effects are weak and the isoplanatic patch size is large at high frequencies, therefore source switching cycles of several minutes and large angular separations are acceptable. However, the ionospheric isoplanatic patch size is difficult to characterize exactly, as it is very variable in time and in Earth location. Nevertheless if the ionosphere is smooth, the calibrator source should not need to be close, certainly not as close as for PR. Extrapolating from PR astrometric errors, a 10° or even 20° ionospheric patch size is possible. Therefore, unlike as in PR, the conditions for finding a suitable SFPR calibrator source are much less restrictive.

Since the calibrator scans reduce the observing time on the target source, we advise scheduling the observations to achieve a reasonable (i.e. to the level of other error contributions) ionospheric calibration, following Eqs. 10 and 11, with the minimum calibration overhead.

4.3. *Target/Calibrator Source fluxes*

A necessary condition for successful application of SFPR techniques is that the calibrator and target sources must be directly detected at the reference frequency scans (i.e. within the coherence time imposed by the tropospheric fluctuations). Typical minimum source flux values are the same as for the calibrator source in conventional PR observations at the reference frequency ν^{low} . On the other hand, direct detections at the target frequency ν^{high} are not a requirement, since the tropospheric calibration using dual-frequency observations results in phase stabilization at the target frequency, for both sources. This enables increased sensitivity through use of longer integration times (i.e. up to several minutes) in the self-calibration of the troposphere-free calibrator dataset. Finally, the SFPR-calibrated target dataset is expected to reach an extended coherence time up to \sim hours, as in conventional PR.

The effect of the source fluxes into the final errors is described by the theoretical thermal noise limit (as shown in Eq. 12). Along with the source flux, other parameters that define this limit are the receiver noise (SEFD) and the frequency ratio R . For example, to compare the thermal noise errors in SFPR observations at 86 GHz either using 22 or 43 GHz as the reference frequency, one should take into account the effect of halving R compared to that of the increased SEFD at 43 GHz. For the current VLBA parameters one needs to balance the 40% reduction from the frequency-ratio contribution against the approximately three-fold higher SEFD, for 43-GHz compared to 22-GHz. Additionally one needs to account for the fact that the sources tend to be weaker at higher frequencies.

5. **Observational demonstration**

5.1. *Observations and Data Analysis*

On February 18, 2007, we carried out SFPR observations at 43 and 86 GHz, using the eight antennas of the NRAO Very Long Baseline Array (VLBA) which are equipped for the highest frequencies, for a total of 7 hours. Based on the encouraging results from our error analysis, we selected as targets two pairs of well known and bright AGNs, with very different angular separations: a close pair, 1308+326 & 1308+328, 14' apart, and a widely separated pair, 3C273 & 3C274 (M87), 10° apart. These source configurations provide two extreme cases of application of SFPR techniques, and allow us to investigate the effect of the source pair angular separation in our method. Table 2 lists the theoretical error contributions estimated for these observations.

All sources were observed in the same run (*Exp. Code: BD119*), alternating ~ 1.5 -hour long blocks on each of the source pairs to improve the coverage of the (u, v) -plane. For each source pair, the observations consisted of alternating pointings between the two sources (with a switching cycle of ~ 5 minutes), and a rapid frequency-switching between 43 and 86 GHz (with a switching cycle of ~ 60 seconds). Hence, for a given source, the scan durations at each frequency were ~ 20 seconds long, as the time to change receivers at the VLBA is ~ 10 seconds. The observing switching cycles were chosen to match the temporal scale of the ionospheric and tropospheric fluctuations estimated for “good” weather conditions, respectively, as requested for this experiment. This results in a total on-source time equal to ~ 30 minutes, for each source at each frequency, after subtracting the receiver and telescope slew times, and time devoted to pointing and other basic calibration.

Additionally, a series of 1-hour long test observations (*Exp. Code: BD123*) were run on different days in February and March, 2007, using a similar observing schedule but with no weather restrictions to test the robustness of the method weather-wise. In this case only the close pair of sources were observed because of time constraints. In all cases, each antenna recorded eight 16-MHz IF channels, using 2-bit Nyquist sampling, which resulted in a data rate of 512 Mbps.

We used the NRAO AIPS package for the data reduction. We followed standard VLBI calibration procedures for correcting for updated Earth Orientation Parameters, GPS-measured TEC values, amplitude and feed-rotation calibration (see Dodson & Rioja (2009) for details). The astrometric analysis was carried out independently for each pair of sources following a common two-step calibration strategy, as explained in Section 2, with 1308+326 and 3C274 as target sources, 1308+328 and 3C273, as calibrator sources, and 86 and 43 GHz as the target (*high*) and reference (*low*) frequencies, respectively. First, we used the same-source observations at the two frequencies to eliminate the dominant rapid tropospheric phase fluctuations at 86 GHz, followed by a second calibration cycle to correct for weaker, slower, remaining ionospheric and instrumental contributions in the target data, using the observations of the calibrator source.

Some details on the implementation of SFPR using AIPS are described here (see Dodson & Rioja (2009) for more information). We used the AIPS task FRING to estimate the residual antenna-based phases and phase derivatives (delay and rate) at 43 GHz, for each source and for each scan of duration ~ 20 seconds, using a point-source model. The extended source structure contribution was removed using hybrid maps as input models to CALIB, on the FRING-ed data, for the 3C sources. The SN-tables generated by the FRING and CALIB tasks provide the basis for the subsequent calibration of the 86-GHz data sets, once the estimated phase values have been scaled by 2 (i.e. the frequency ratio). The phase-scaling operation

can be done with the SNCOR task, using the function ‘XFER’ (although it is meant for a different purpose); for the delay and rate values, which are stored in frequency-independent units of seconds and seconds/second respectively, no changes are required. Then, the entries in the SN-tables were interpolated between consecutive 43-GHz scans, 60 seconds apart, with the task CLCAL, and applied to calibrate the interleaving observations of the same source at 86 GHz. The result of this dual-frequency calibration are tropospheric-free (or FPT-calibrated) datasets with increased coherence time at 86 GHz, for both sources of each pair. However the remaining errors prevent the recovery of the position of the target source, using a Fourier inversion, at this stage.

To recover the astrometry a further calibration iteration is required, to disentangle the “core-shift” signature from the remaining dispersive contributions in the tropospheric-free or FPT-calibrated dataset at 86-GHz, along with the source structure contribution. To do this in AIPS, we re-FRING the FPT-calibrated 1308+328 and 3C273 calibrator datasets at 86 GHz, and applied the interpolated adjusted antenna phase, delay and rate solutions to the FPT-calibrated 1308+326 and 3C274 target datasets at 86 GHz, respectively. The resultant SFPR-calibrated data-sets were Fourier inverted and deconvolved with IMAGR, without further calibration, to produce the SFPR-maps for both target sources at 86 GHz.

5.2. Observational Results

The application of SFPR techniques results in a SFPR-ed map of the target source, where the offset of the peak in the brightness distribution with respect to the center of the map is astrometrically significant. As in conventional PR, the price to pay for preserving the astrometric signature is that the quality of the reconstructed image is degraded as compared to those in hybrid maps, due to residual calibration errors. Nevertheless these degraded images retain the astrometric information.

Table 2 lists the theoretically estimated *rms* phase error contributions for our SFPR observations at 43/86 GHz of 2 pairs of sources with very different angular separations, 14' and 10° respectively, using the VLBA. Note that the so-called *static* ionospheric errors are significantly higher for the pair with larger separation, while the dominant *dynamic* tropospheric errors, which depend on the frequency switching cycle and weather conditions, are similar for both pairs. All error values have been calculated using the formulae from the error analysis (section 3) and predict a successful outcome, albeit with reduced peak flux. This is confirmed by the SFPR-maps presented in this section, which provide an empirical demonstration of the feasibility of SFPR techniques for “bona fide” astrometry, even with very wide source angular separations.

Figures 2 and 3 show the hybrid maps for all observed sources at 43 and 86 GHz. The peak flux from these maps will be used for calculating the flux recovery quantity, or Strehl ratio, which is defined as the ratio between the peak fluxes in the SFPR-maps and hybrid maps. This relates to the variance of a random Gaussian phase noise, σ_ϕ , as $e^{-\sigma_\phi^2/2}$ (Thompson et al. 2001). Therefore it provides an empirical estimate of the magnitude of the random errors in the SFPR-maps, and of the corresponding astrometric precision. Nevertheless this approach is not sensitive to systematic errors, which could potentially bias the astrometric accuracy, and further error analysis, as presented in Section 3, is required to provide a reliable error estimate.

Figure 4 shows the SFPR-image of 1308+326 at 86 GHz. This map was made using the calibration derived from the BD119 observations of the same source at 43-GHz and further corrections derived from observations of 1308+328, 14' away, as described above. The peak flux in the SFPR-image is 84 mJy, which corresponds to a $\sim 38\%$ flux recovery, equivalent to a *rms* phase error of ~ 1.4 radians. The observational error estimate is in good quantitative agreement with the theoretical predictions from our error analysis, as listed in Table 2, which arise from residual short term tropospheric temporal fluctuations (i.e. *dynamic* tropospheric errors) and a frequency switching cycle of ~ 1 minute. The effect of these errors is expected to produce degraded images, with the image signal-to-noise ratio reduced by the random phase noise. For comparison, the only conventional PR map which has been done at 86-GHz (Porcas & Rioja 2002), using this same pair of sources, resulted in a flux recovery of only 20%. However, the peak of brightness in the map would not be shifted, hence the astrometric errors are expected to be small, under $30 \mu\text{as}$, for the given phase noise and assuming a synthesized beam $\sim 150 \mu\text{as}$. We measured the offset of the peak of brightness in the SFPR-map with the AIPS task JMFIT to be $22 \mu\text{as}$ along a PA= -142° , with a formal fitting error of $13 \mu\text{as}$. Therefore we conclude that there is no significant astrometric offset in our SFPR-map. The results from previous astrometric observations of this pair of sources (Rioja et al. 1996; Rioja & Porcas 1996; Porcas & Rioja 2000) at lower frequencies are compatible with a zero core-shift between 43 and 86 GHz, as found in our analysis.

The multiple 1-hour long observations (BD123), carried out on different days, of the 1308+326 and 1308+328 pair allowed us to check the repeatability of the astrometric results and characterize the robustness of the method with respect to weather. We found that in poor weather conditions the flux recovery fell dramatically, as expected, since the frequency switching time was insufficiently fast to follow the tropospheric fluctuations. However, in all cases most baselines could be calibrated, and the positions of the peak of brightness in the SFPR-maps at 86 GHz were distributed around the center of the map, with an average position and *rms* equal to $20 \pm 17 \mu\text{as}$. Based on this repeatability we conclude that the

astrometric measurements using SFPR techniques are robust in various weather conditions. Additionally, this repeatability serves to give a realistic error estimate of the astrometric precision achieved at 86 GHz using SFPR techniques, for a close pair of radiosources, of the order of $\sim 20 \mu\text{as}$.

Figure 5 shows the SFPR-image of 3C274 at 86 GHz. This map was produced using the calibration derived from the BD119 observations of the same source at 43-GHz and further corrections derived from observations of 3C273, 10° away. The larger angular separation between the sources in the 3C pair, compared to the $14'$ for the 1308+32 pair, along with the lower declination and the North-South relative orientation, makes this case the ultimate limit of what we would consider to be a suitable SFPR calibrator. We note that if the goal was to make accurate phase referenced maps, rather than test the calibration scheme, M84 ($\sim 1.4^\circ$ away from 3C274) would be a more suitable calibrator source. The peak flux in the SFPR-image is 150 mJy, which corresponds to a $\sim 32\%$ flux recovery compared to the peak in the hybrid map, which is equivalent to a *rms* phase error of ~ 1.5 radians. This is similar to the flux recovery for the close pair, and in agreement with the theoretical estimates from our error analysis (Table 2), since the dominant errors (i.e. $\sigma\phi_{\text{dtrp}}$) are only slightly dependent on the source separation and both pairs were observed under identical weather conditions. On the other hand, the larger separation between the two sources of this pair results in a significant residual “static” ionospheric error (see Table 2), which is expected to propagate into astrometric errors. Also we find differences in the astrometric estimates which depend on the inclusion of data from the MK antenna or not, presumably since it provides the longest baselines, and includes the lowest antenna elevations. Leaving out the MK data, the offset of the peak of brightness with respect to the center in the SFPR-map, measured with JMFIT, is $43 \mu\text{as}$ along a $\text{PA}=+160^\circ$, with formal fitted errors $30 \mu\text{as}$; this shift was doubled in magnitude when we include MK data in the analysis.

In the absence of any other astrometric observations at 86 GHz to compare our results against, we consider here three scenarios to interpret the measurements in the SFPR-map. Firstly, any apparent source position shifts resulting from differential structure blending effects from observations at different frequencies, or real shifts due to opacity changes (true “core-shifts”), are expected to occur up stream along the jet structure axis. The source axis for 3C273 is along $\text{PA} \sim -142^\circ$ (Fig. 3), for 3C274 we consider a range of PAs between $\sim -90^\circ / -45^\circ$ derived from our maps (Fig. 3) and larger scale maps, respectively. The SFPR analysis measures the relative position shift in 3C274 between 86 and 43 GHz, with respect to that in 3C273. Hence, given the orientation of the expected shifts at each source, the combined shift is expected to appear in a range of PAs between $+90^\circ / +135^\circ$ (if dominated by 3C274) and -142° (if dominated by 3C273), depending on the magnitudes of the individual contributions. The direction of the measured shift in the SFPR-map (Fig.

5), along PA $\sim -164^\circ$, falls in this range. Secondly, we use the theoretical predictions for the core-shifts between 43 and 86 GHz for these sources to estimate the corresponding offset in the SFPR-map. These are $65 \mu\text{as}$ (Lobanov 1998) for 3C273, and zero for 3C274 (Lobanov, personal comms.), which correspond to an offset in the SFPR-map of $\sim 65 \mu\text{as}$ along PA $\sim -142^\circ$. This theoretical position is $\sim 55 \mu\text{as}$ away (approximately 2σ , based on the formal JMFIT errors) from that measured in the SFPR-map shown in Figure 5. Finally, we consider the propagation of astrometric errors in the analysis. The residual systematic long-term ionospheric errors, as listed in Table 2, are expected to propagate into the astrometry. The simulation studies carried out by Pradel et al. (2006) show that the dominant propagation of astrometric errors, in PR observations, are along the declination coordinate for pairs of sources with low declination and North-South relative orientation, as it is the case for 3C273/3C274. Leaving aside the differences between the observational methods, and extrapolating their findings to SFPR, all or part of the measured offset in the SFPR-map could be due to this effect.

In conclusion, as we are unable to compare our findings with other experimental results from any other technique, we propose to use the observed shift in the SFPR-map as an upper bound for the astrometric uncertainties in the analysis method, when the angular separations are of many degrees. That is, we give a conservative upper bound of 0.1 mas to the astrometric accuracy at 86 GHz using SFPR techniques, in the case of two sources with a separation of $\sim 10^\circ$.

6. Discussion

6.1. Validation of SFPR method:

We have developed a new two-step calibration technique called SFPR that, by precisely compensating for the effect of the propagation medium in VLBI observations, enables high precision astrometry even at the highest frequencies where conventional PR techniques fail. Previous attempts using fast frequency-switching observations achieved an increased coherence time as a result of the dual-frequency tropospheric calibration, which enabled the detection of weak sources but failed to provide astrometry due to remaining dispersive errors (Middelberg et al. 2005). Our method addresses this issue with a second calibration step, that corrects for those and hence enables astrometry. We have provided experimental demonstration of the ability of the SFPR method to disentangle the astrometric signature from the other contributions using VLBA observations at 86 GHz, the highest VLBA frequency, and 43 GHz. This “chromatic” astrometric signature corresponds to the angular separation between the emitting regions at the two observing frequency bands in the target

source, assuming an achromatic calibrator. Therefore, our SFPR method is a valuable tool for studies that require comparison and *bona-fide* astrometric registration of images at two or more frequencies, even at the highest frequencies possible with VLBI. Additionally, when combined with conventional PR observations at ν^{low} , SFPR can provide ‘PR-like’ astrometry at ν^{high} . That is, measurements of the positions with respect to an external calibrator. Such astrometric measurements can be used for position stability, proper motion and parallax studies at frequencies beyond the traditional limit of phase referencing (~ 43 GHz). In summary this method offers the means to expand the benefits that conventional PR techniques offer in the moderate frequency regime, into the highest frequencies used in VLBI. In previous works dual frequency observations have been used for the detection of weak sources at mm-VLBI; now, with the SFPR technique, *bona-fide* high precision astrometric mm-VLBI (and sub-mm) can also be performed.

We have carried out an analytical error analysis to characterize the performance of the SFPR method. This analysis shows that when using frequency-switching observations the dominant source of errors are the random fluctuations in the *dynamic* component of the troposphere. Also that the magnitude of this error depends on the frequency switching cycle at the observations and the weather conditions, irrespective of the pair angular separation. These findings are in good qualitative and quantitative agreement with the experimental results from our SFPR observations of two pairs of sources with very different angular separations. This validates the new astrometric method and the error analysis, confirming its potential in mm-VLBI. Furthermore it gives confidence in our extrapolations into domains yet untested, that is to the sub-mm regime, and to simultaneous dual frequency observations.

6.2. *Broad scope of application:*

The constraints for successful SFPR observations are relatively easy to fulfill. The SFPR method has been successfully demonstrated with VLBA observations of a pair of sources with a large (10°) angular separation, at 43/86 GHz. These results are encouraging as they suggest that the SFPR method would work with any other combination of integer-ratio frequencies provided suitable frequency switching cycles are used, and that the angular separation between the calibrator and target sources can be large and telescope switching cycles long; certainly much more than those required for conventional PR. The key elements for success of the new method in the high frequency regime are, firstly, that the frequency switching operation in SFPR can be carried out much faster than the source switching counterpart in PR. Secondly, that finding a suitable SFPR calibrator source is relatively easy, unlike for PR, because wider angular separations and longer switching cycles are allowable, along with

the extended coherence at the high frequencies. The SFPR method can be implemented as a regular observing mode with existing instruments, such as the VLBA, which support fast frequency switching operations. The best astrometric performance is achieved when multiple frequency bands can be observed simultaneously, as this provides an exact tropospheric correction in all weather conditions, eliminates the need of phase connection and increases the on-source time. The Korean VLBI Network (KVN), equipped with multi-channel receivers at 22/43/86/129 GHz, and telescopes like Yebes and Haystack are among the instruments that can carry out simultaneous observations of multiple high frequency bands to achieve maximum benefit from the SFPR technique. Based on our analysis it is clear that simultaneous frequency observations can be very useful in high frequency VLBI. We strongly suggest that this capability is included in all next-generation instruments. We conclude that this method is broadly applicable to mm-VLBI observations of many target sources, and unique in providing *bona-fide* astrometrically registered images and high precision relative astrometric measurements using existing and newly built instruments.

6.3. Applications to space-VLBI:

Additionally to the errors in the atmospheric propagation models, the geometric errors also introduce inaccuracies in the PR analysis, which can ultimately prevent its application. While for VLBI ground arrays the telescope coordinates can be accurately measured with dedicated geodesy campaigns this is of particular concern for space-VLBI observations, since the precise orbit determination for a satellite antenna is much more complicated. For example, for VSOP-2, the accuracy in the orbit reconstruction required for successful PR observations at 43 GHz must be better than 10-cm (A07), which is challenging. For comparison, the typical orbit determination accuracy for its predecessor, the HALCA satellite, was 2–5 meters using Doppler measurements from the Ku-band link (Porcas et al. 2000; Rioja et al. 2009). Strategies to achieve the 10-cm level of accuracy using global satellite navigation systems and satellite laser ranging techniques are presented in Asaki et al. (2008).

Alternatively, the SFPR method automatically corrects for any geometric errors, including any orbit determination errors, irrespective of their magnitude. There are no specific requirements on the orbit accuracy for SFPR analysis other than those imposed by the correlator fringe field of view, which is typically many meters. In addition to the astrometric applications, the increased sensitivity resulting from longer coherence time is very useful because of the limited size of an orbiting antenna, particularly at the higher frequencies. Also, the fast frequency-switching operation for SFPR is less demanding than fast source-switching for PR, reducing the requirements on the satellite attitude control system. Further discus-

sions can be found in Rioja & Dodson (2009). Therefore, we believe this method will be very useful for space VLBI missions. In particular, applied to VSOP-2 observations, it would enable increased sensitivity allowing the detection of weaker sources, and permit astrometric measurements and long term monitoring projects at 43 GHz, by using the calibration derived from interleaving observations at 22 GHz even with a coarse orbit determination. For other future space VLBI missions at high frequencies, e.g. “Millimetron” (Wild et al. 2007), having simultaneous observations at multiple frequencies combined with all or some aspects of the SFPR calibration techniques would enable enhanced sensitivity and astrometric capabilities.

6.4. Astrometric Precision & Applications

High precision astrometric and sensitive measurements are valuable tools to provide insight into astrophysical phenomena, as demonstrated by application of phase referencing techniques at a moderate frequency regime (i.e. up to 43 GHz). The SFPR method enables such measurements in the high frequency regime by means of an improved atmospheric calibration. Our analytical error analysis shows that the tropospheric *static* component is readily compensated using SFPR techniques and that, in general the *dynamic* component would be the dominant source of errors with fast frequency switching observations, leading to \sim a few tens of micro-arcseconds astrometric precision. Based on the repeatability of results from observations with the VLBA we estimate an astrometric precision of $\sim 20 \mu\text{as}$. With simultaneous dual frequency observations both the *static* and *dynamic* components of the troposphere would be precisely compensated, and the much smaller ionospheric residuals become the dominant source of errors. Increasing the reference frequency can result in negligible ionospheric residuals, therefore SFPR techniques at high frequencies offer the prospect of achieving the theoretical astrometric precision set by the interferometer beam size and the signal-to-noise ratio (Thompson et al. 2001).

SFPR techniques applied to VLBI spectral line maser observations would allow a precise *bona-fide* astrometric spatial registration of, for example, the SiO emission structures at different frequency bands (43, 86, 129 GHz) in the same source for studies of the circumstellar environment in AGB stars. When applied to AGN studies, mm and sub-mm VLBI observations probe the inner-jet regions. SFPR can add the measurement of core-shifts with micro-arcsecond precision, plus enable deeper observations for the detection of weak sources. For astrometric measurements relative to an external reference, in combination with conventional PR at ν^{low} , the final precision would be the quadratic sum of errors from both techniques. This would allow the application to proper motion studies of maser emission at the high frequencies, and precise astrometric monitoring programs of the ‘jet foot-prints’ to

unveil the cause of the observed jet-wobbling phenomena.

Acknowledgments

RD acknowledge support for this research by a Marie Curie International Incoming Fellowship within the EU FP6 under contract number MIF1-CT-2005-021873, undertaken at the OAN. VLBA is operated by the National Radio Astronomy Observatory, which is a facility of the National Science Foundation operated under cooperative agreement by Associated Universities, Inc.

REFERENCES

- Alef, W. 1988, *The Impact of VLBI on Astrophysics and Geophysics*, 129, 523
- Asaki, Y., et al. 2007, *PASJ*, 59, 397
- Asaki, Y., Takeuchi, H., & Yoshikawa, M. 2008, in *Proc. of ION GNSS*
- Beasley, A. J., & Conway, J. E. 1995, in *Astronomical Society of the Pacific Conference Series*, Vol. 82, *Very Long Baseline Interferometry and the VLBA*, ed. J. A. Zensus, P. J. Diamond, & P. J. Napier, 328
- Blandford, R. D., & Konigl, A. 1979, *ApJ*, 232, 34
- Dodson, R., Edwards, P. G., & Hirabayashi, H. 2006, *PASJ*, 58, 243
- Dodson, R., & Rioja, M. 2009, *Astrometric calibration of mm-VLBI using Source Frequency Phase Referenced observations*, VLBA Scientific Memo 31, NRAO
- Falcke, H., Melia, F., & Agol, E. 2000, *ApJ*, 528, L13
- Fomalont, E. 1995, in *Astronomical Society of the Pacific Conference Series*, Vol. 82, *Very Long Baseline Interferometry and the VLBA*, ed. J. A. Zensus, P. J. Diamond, & P. J. Napier, 364
- Honma, M., et al. 2003, *PASJ*, 55, L57
- Honma, M., Tamura, Y., & Reid, M. J. 2008, *PASJ*, 60, 951
- Jung, T., Sohn, B. W., Kobayashi, H., Sasao, T., Hirota, T., Kameya, O., Choi, Y. K., & Chung, H. S. 2008, in *The role of VLBI in the Golden Age for Radio Astronomy*

- Kim, H. G., Han, S. T. & Sohn, B. W. 2007, in *Exploring the Cosmic Frontier*, 37, 41
- Lobanov, A. P. 1998, *A&A*, 330, 79
- Middelberg, E., Roy, A. L., Walker, R. C., & Falcke, H. 2005, *A&A*, 433, 897
- Porcas, R. W., Rioja, M. J., Machalski, J., & Hirabayashi, H. 2000, in *Astrophysical Phenomena Revealed by Space VLBI*, ed. H. Hirabayashi, P. G. Edwards, & D. W. Murphy, 245
- Porcas, R. W., & Rioja, M. J. 2000, in *Proceedings of the 14th EVGA meeting*, p. 123
- Porcas, R. W., & Rioja, M. J. 2002, in *Proceedings of the 6th EVN Symposium*, ed. E. Ros, R. W. Porcas, A. P. Lobanov, & J. A. Zensus, 65
- Porcas, R. W., & Rioja, M. J. 2002, in *Proceedings of the 16th EVGA meeting*, p. 121
- Pradel, N., Charlot, P., & Lestrade, J. 2006, *A&A*, 452, 1099
- Reid, M. J., & Brunthaler, A. 2004, *ApJ*, 616, 872
- Rioja, M. J., Porcas, R. W., & Machalski, J. 1996, in *IAU Symposium, Vol. 175, Extragalactic Radio Sources*, ed. R. D. Ekers, C. Fanti, & L. Padrielli, 122
- Rioja, M. J. & Porcas, R. W., 1996, in *Proc. 11th EVGA meeting*, p. 219
- Rioja, M., & Dodson, R. 2009, *Multi-frequency ASTROMETRY with VSOP-2: An Application of Source/Frequency Phase Referencing techniques*, VLBA Scientific Memo 32, NRAO
- Rioja, M., Porcas, R., Dodson, R., & Asaki, Y. 2009, in *Astronomical Society of the Pacific Conference Series, Vol. 402, Astronomical Society of the Pacific Conference Series*, ed. Y. Hagiwara, E. Fomalont, M. Tsuboi, & M. Yasuhiro, 486
- Rioja, M. J., Dodson, R., Kamohara, R., Colomer, F., Bujarrabal, V., & Kobayashi, H. 2008, *PASJ*, 60, 1031
- Rioja, M. J., Dodson, R., Porcas, R. W., Suda, H., & Colomer, F. 2005, *ArXiv Astrophysics e-prints astro-ph/0505475*
- Shapiro, I. I., et al. 1979, *AJ*, 84, 1459
- Soria-Ruiz, R., Alcolea, J., Colomer, F., Bujarrabal, V., & Desmurs, J.-F. 2007, *A&A*, 468, L1

- Thompson, A. R., Moran, J. M., & Swenson, G. W. 2001, *Interferometry and Synthesis in Radio Astronomy* (New York, Wiley-Interscience, 2001, 692 p.)
- Ulvestad, J. 1999, Phase-referencing cycle times, VLBA Scientific Memo 20, NRAO
- Walker, C. 1995, in *Astronomical Society of the Pacific Conference Series*, Vol. 133, *Very Long Baseline Interferometry and the VLBA*, ed. J. A. Zensus, P. J. Diamond, & P. J. Napier, 247
- Wild, W., et al. 2009, *Exp. Ast.*, 23, 221

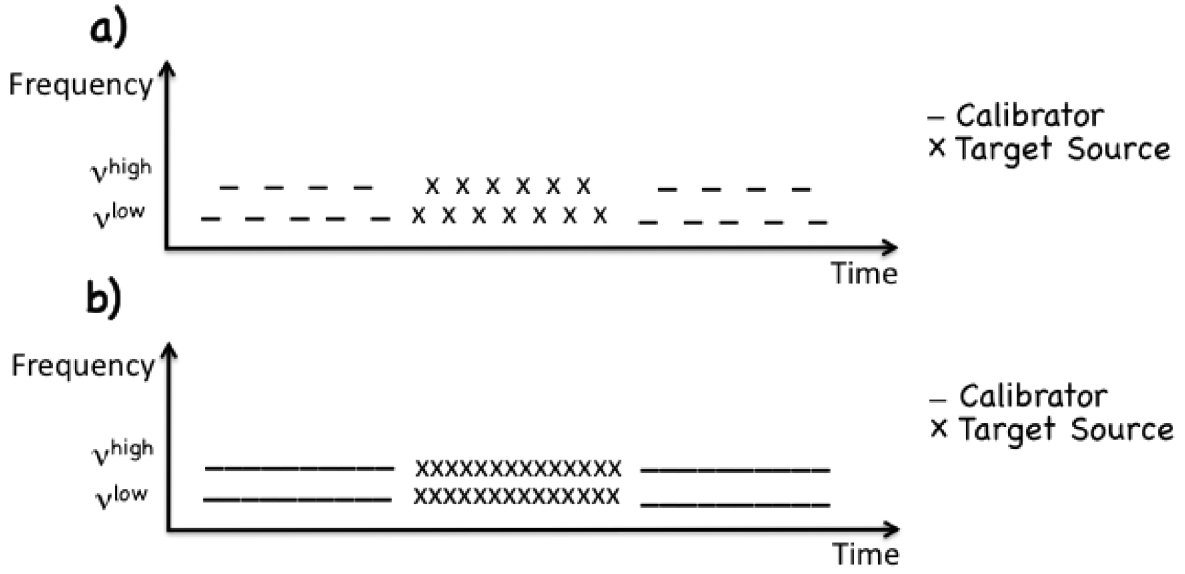


Fig. 1.— A sketch showing the distribution of observing time per frequency and per source (typically minutes), in SFPR observations using: a) fast frequency-switching with slow source-switching, and b) simultaneous dual-frequency observations with slow source-switching.

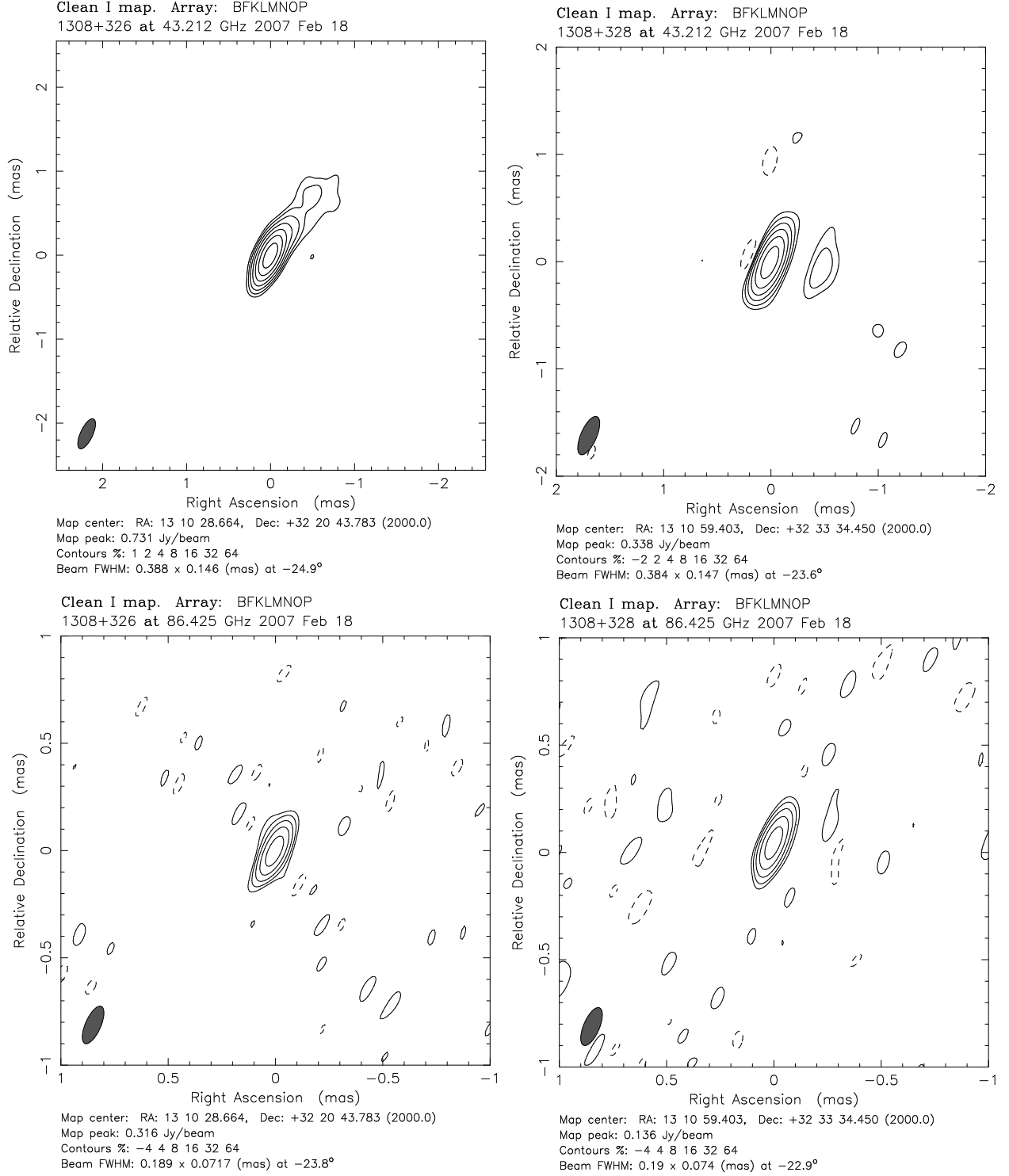


Fig. 2.— Hybrid maps of 1308+326 (left) and 1308+328 (right) at 43 (top) and 86 GHz (bottom). The data have been exported from AIPS and all antennas selfcalibrated and imaged with uniform weighting in difmap.

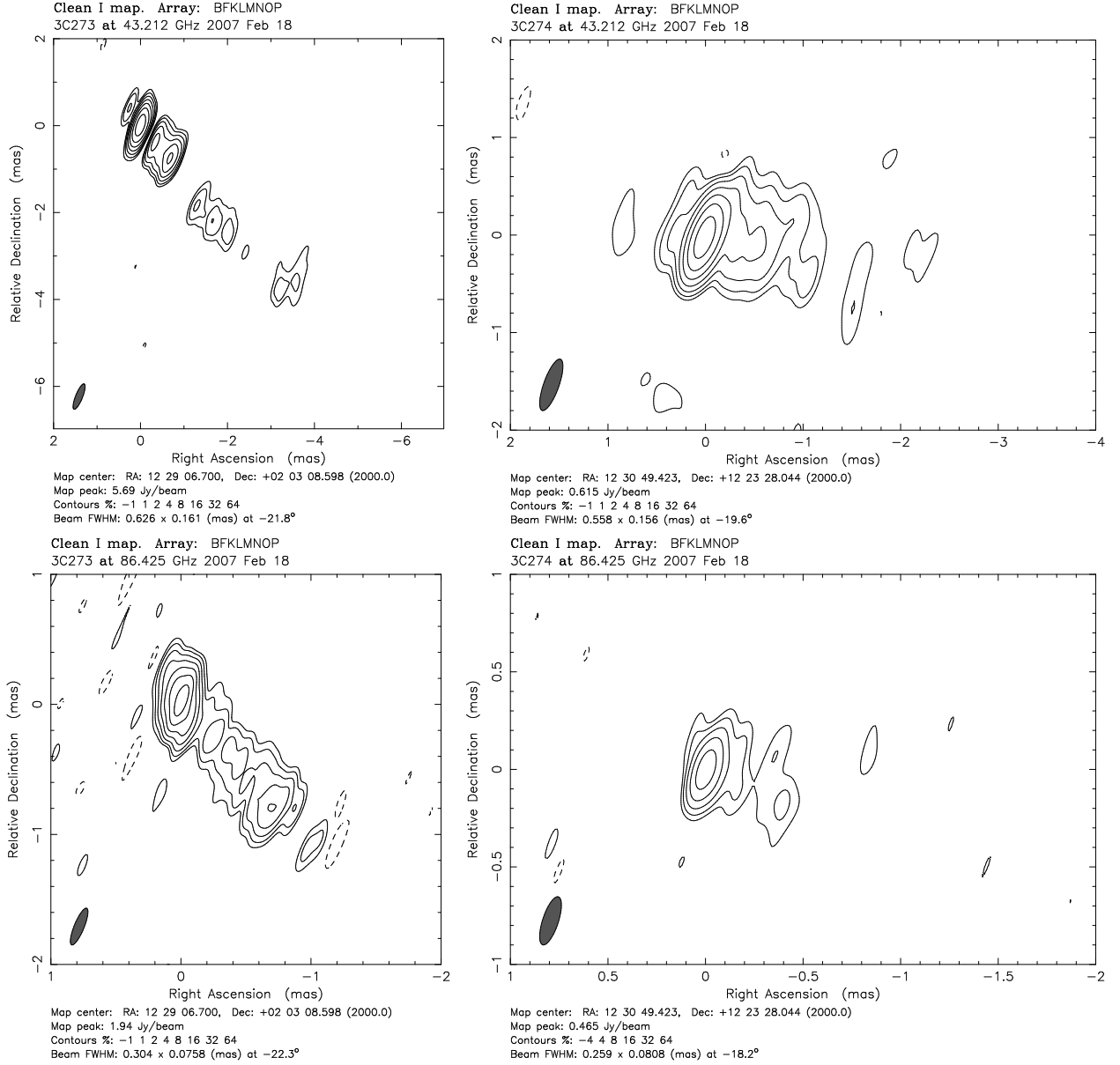


Fig. 3.— Hybrid maps of 3C273 (left) and 3C274 (right) at 43 (top) and 86 GHz (bottom). The data have been exported from AIPS and all antennas selfcalibrated and imaged with uniform weighting in difmap.

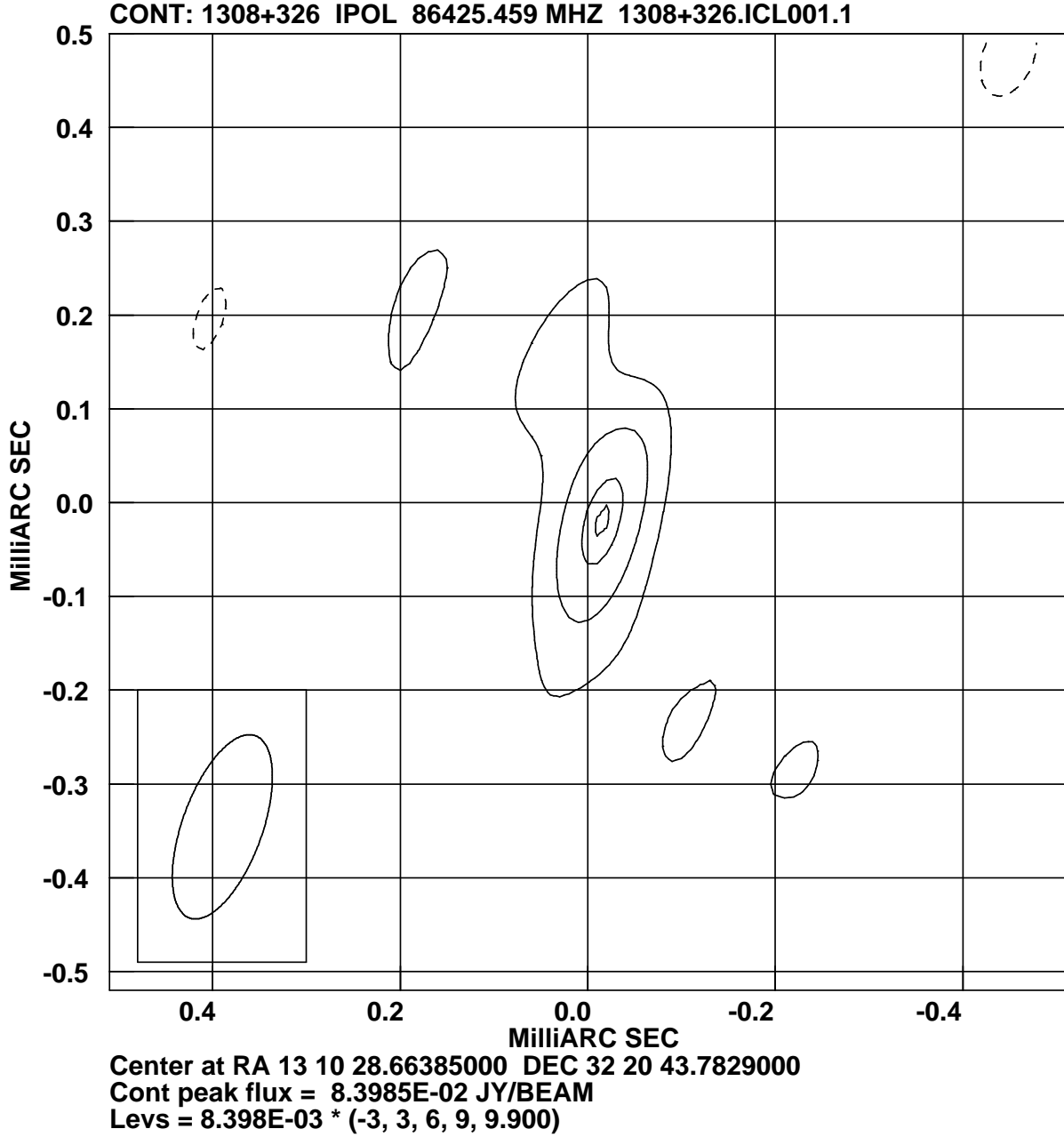


Fig. 4.— Source-Frequency Phase Referenced (SFPR-ed) map of 1308+326 at 86 GHz from BD119, from VLBA observations at 43 and 86 GHz, along with a calibrator source, 1308+328, 14' away. The *rms* noise level of the map is 9 mJy/beam. The flux recovery is 38%. An astrometric offset of $22 \pm 13 \mu\text{as}$ is measured, which is not significant. Previous observations of this pair of source (see text) are compatible with a zero core-shift between 43 and 86 GHz, as seen in this image. We estimate an astrometrical error of $\sim 20 \mu\text{as}$ for SFPR observations with a close pair of sources.

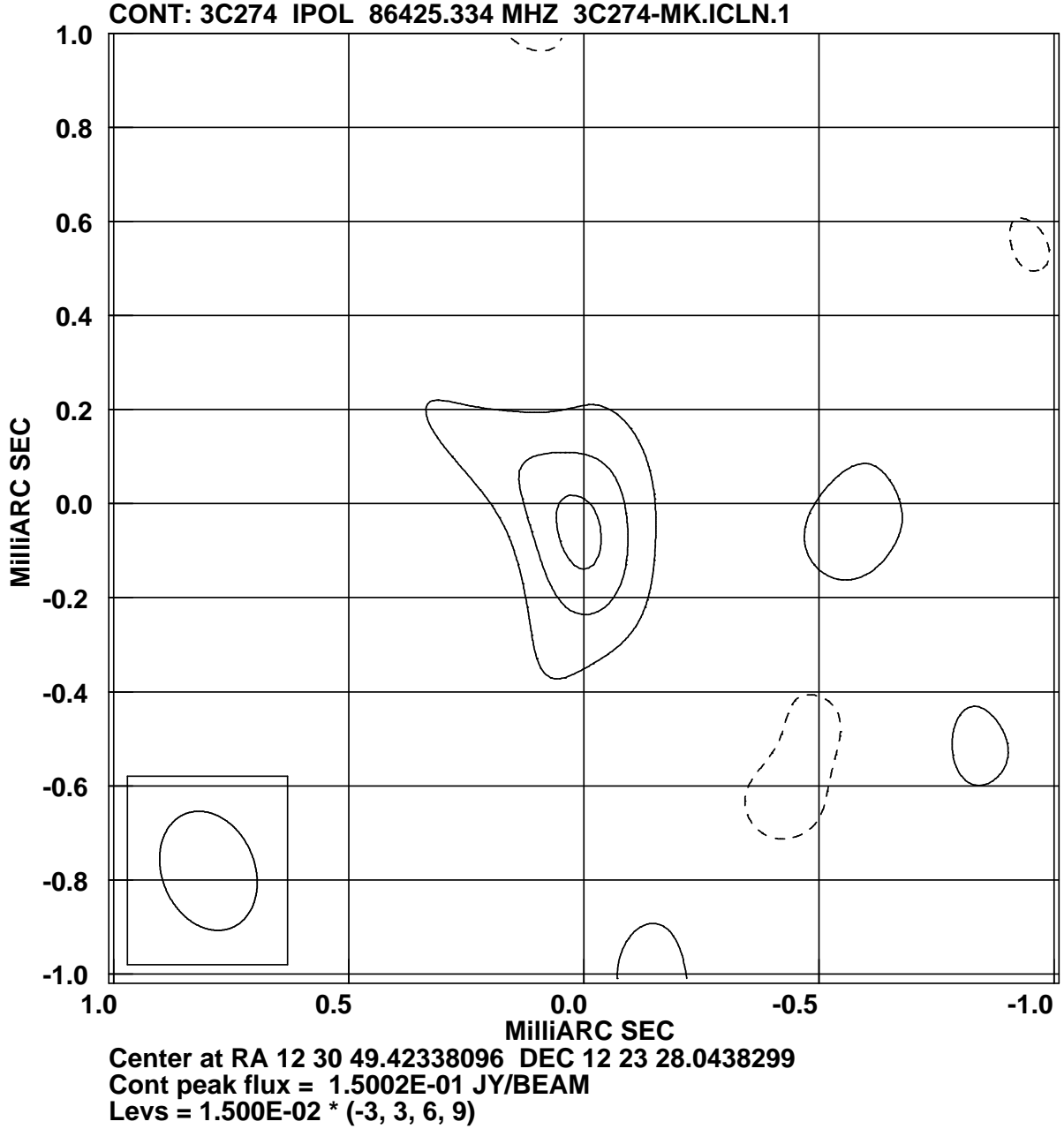


Fig. 5.— Source-Frequency Phase Referenced (SFPR-ed) map of 3C274 at 86 GHz from BD119, from VLBA observations at 43 and 86 GHz, along with a calibrator source, 3C273, 10° away. The data from MK antenna have been edited out. The *rms* noise level of the map is 18 mJy/beam. The flux recovery is 32%. The direction of the astrometric offset (160°) of the peak-flux with respect to the center of the map is compatible with that expected from the core shift, and its magnitude ($48 \pm 30 \mu\text{as}$) is consistent with theoretical predictions for these sources. However it also agrees with expected propagation of astrometric errors. In the absence of other observations to compare our results with, we propose to use the offset of the peak of brightness with respect of the center of the SFPR-map as a conservative upper limit for the astrometric accuracy achieved with SFPR techniques applied to pairs of sources with wide angular separation.

Table 1: Estimated residual phase error budget for Source-Frequency Phase Referencing (SFPR) techniques, per baseline, using the formulae in Section 3. For comparison we include the error budget estimates for Phase Referencing (PR) techniques at 43 GHz, using formulae in A07. For SFPR the errors correspond to those at the higher frequency. In all cases weather conditions were set to ‘good’ and the tropospheric zenith delay error $\Delta l_z = 3$ cm (except when marked with ^(b), then 1 cm). All other parameters are set to the nominal values in the equations.

Error term		RMS phase [deg]				
		SFPR _{43→86GHz}		SFPR _{43→129GHz}		PR _{43GHz}
		SOURCE/FREQ. SWITCHING (1)	ONLY SOURCE SWITCHING (2)	SOURCE/FREQ. SWITCHING (3)	ONLY SOURCE SWITCHING (4)	SOURCE SWITCHING (5)
Dynamic Troposphere	$\sigma\phi_{\text{dtrp}}^{\text{high}}$	76	0	115	0	43
Static Troposphere	$\sigma\phi_{\text{strp}}^{\text{high}}$	0	0	0	0	107 (36 ^b)
Dynamic Ionosphere	$\sigma\phi_{\text{dion}}^{\text{high}}$	1 (2 ^a)	1 (2 ^a)	2 (3 ^a)	2 (3 ^a)	0.3
Static Ionosphere	$\sigma\phi_{\text{sion}}^{\text{high}}$	6 (29 ^a)	6 (29 ^a)	10 (51 ^a)	10 (51 ^a)	4
Geometric ^c	$\sigma\phi_{\text{geo}}^{\text{high}}$	0	0	0	0	30
Thermal Noise ^d	$\sigma\phi_{\text{thermal}}^{\text{high}}$	1.5	1.5	2.6	2.6	0.2
SUM		77 (82 ^a)	6 (29 ^a)	115 (125 ^a)	10 (51 ^a)	120 (63 ^b)

(1): SFPR observations at 43 and 86 GHz, using *frequency and source switching*, with frequency switching cycle $T_{\text{swt}}^\nu = 60$ seconds, and source switching cycle $T_{\text{swt}} = 300$ seconds. The source switching angles are $\Delta\theta = 2^\circ$ and $\Delta\theta = 10^\circ$, with values for the later in brackets and labelled with ^(a) if different from those for the former. **(2):** SFPR observations at 43 and 86 GHz, using simultaneous dual frequency observations and *only source switching*, with a (source switching) cycle $T_{\text{swt}} = 300$ seconds. The source switching angles are $\Delta\theta = 2^\circ$ and $\Delta\theta = 10^\circ$, with values for the later in brackets and labelled with ^(a) if different from those for the former. **(3):** Same as **(1)**, for 43 and 129 GHz. **(4):** Same as **(2)**, for 43 and 129 GHz. **(5):** PR observations at 43 GHz, with a switching angle $\Delta\theta = 2^\circ$ and source switching cycle $T_{\text{swt}} = 60$ seconds. **(a):** Error term for $\Delta\theta = 10^\circ$, given only if different from that for $\Delta\theta = 2^\circ$, for SFPR. **(b):** PR with improved tropospheric calibration strategy to achieve $\Delta l_z = 1$ cm. **(c):** The geometric errors $\sigma\phi_{\text{geo}}$ are a combination of the $\sigma\phi_{\text{bl}}$ and $\sigma\phi_{\Delta s}$ errors with nominal values. **(d):** The $\sigma\phi_{\text{thermal}}$ contribution has been calculated using the SEFD parameter values for the VLBA at 43 and 86 GHz, and for the KVN at 129 GHz, and source fluxes of 0.1 Jy.

Table 2: Estimated residual phase error budget for Source-Frequency Phase Referencing (SFPR) techniques, per baseline, for our observations of the two pairs of sources, at 43/86 GHz (matching BD119). Also, for comparison, estimated errors for PR observations at 86 GHz for the close pair (PR is not feasible for the pair 10° apart). The error values have been calculated using the formulas in this paper, for SFPR, and in A07, for PR. For SFPR the errors correspond to those at the higher frequency. In all cases weather conditions were set to ‘good’ and the tropospheric zenith delay error $\Delta l_z = 3$ cm.

Error term		RMS phase [deg]		
		1308+326/1308+328 $\delta \sim 32^\circ, 14'$ apart		3C273/3C274 $\delta \sim 0^\circ, 10'$ apart
		SFPR	CONVENTIONAL PR	SFPR
		43 \rightarrow 86GHz (1)	86 GHz (2)	43 \rightarrow 86GHz (3)
Dynamic Troposphere	$\sigma\phi_{\text{dtrp}}^{\text{high}}$	68	69	80
Static Troposphere	$\sigma\phi_{\text{strp}}^{\text{high}}$	0	12	0
Dynamic Ionosphere	$\sigma\phi_{\text{dion}}^{\text{high}}$	0.3	0.1	3
Static Ionosphere	$\sigma\phi_{\text{sion}}^{\text{high}}$	0.3	0.1	37
Geometric ^a	$\sigma\phi_{\text{geo}}^{\text{high}}$	0	3	0
Thermal Noise ^b	$\sigma\phi_{\text{thermal}}^{\text{high}}$	0.7	0.5	0.2
SUM		68	70	88

(1): SFPR observations at 43/86 GHz of the pair of sources 1308+326 and 1308+328 using a frequency switching cycle $T_{\text{swt}}^\nu = 60$ seconds, and source switching cycle $T_{\text{swt}} = 300$ seconds. The switching angle is $\Delta\theta = 14'$. Values of parameters Z_g, Z_i, Z_f are $30^\circ, 29^\circ$ and 28° , respectively. **(2):** Conventional PR observations at 86 GHz of the pair of sources 1308+326 and 1308+328, $14'$ away, with a switching cycle $T_{\text{swt}} = 60$ seconds. **(3):** SFPR observations at 43/86 GHz of the pair of sources 3C273/3C274 using a frequency switching cycle $T_{\text{swt}}^\nu = 60$ seconds, and source switching cycle $T_{\text{swt}} = 300$ seconds. The switching angle is $\Delta\theta = 10^\circ$. Values of parameters Z_g, Z_i, Z_f are $50^\circ, 47^\circ$ and 46° , respectively. **(a):** This contribution has been calculated using $\sigma\phi_{\text{bl}} = 0.5$ cm. **(b):** The $\sigma\phi_{\text{thermal}}$ contribution has been calculated using the SEFD parameter values for the VLBA at 43 and 86 GHz (1500 and 4000 Jy, respectively), and the source fluxes are the peak flux measured in the corresponding hybrid maps shown in Figures 2 and 3.